

Three-Dimensional Magnetic Mapping using
Electromagnetically Induced Transparency and the Effects of
Retro-reflected Light on EIT

Jacob A. Fry

Advisor: Irina Novikova

The College of William and Mary

Senior Thesis

April, 13 2012

Abstract

The objective of this project is to create an optical vector magnetometer. When completed, this device will use the EIT resonances of Rubidium vapor to create a three dimensional vector map of an unknown magnetic field. In this paper, we report on two important capabilities of such a device. First, we demonstrate its potential for magnetic field detection of non-transparent targets by retro-reflecting the probe laser back through our target cell. We observe that the electromagnetically induced transparency signals (EIT) change neither frequency nor shape when retro-reflected. Second, we report the direct measurement of both magnitude and direction of an applied magnetic field is possible. We accomplish this by measuring the magnetic field

along two perpendicular directions. Each measurement direction yields a plane that contains \vec{B} , and we show that \vec{B} is the intersection of the two planes.

1 Introduction

1.1 Magnetometer Based Upon EIT

The purpose of this project is to create a high precision, optical magnetometer of small size and expense. We base our magnetometer on an effect observed in atoms called electromagnetically induced transparency (EIT) in which the transmission of a resonant bichromatic laser radiation peaks. This peak occurs when the differential frequency of the laser's frequency components matches the energy splitting of various magnetic sublevels of the ground states. These EIT transmission peaks have relatively high amplitude, a narrow frequency range, and their amplitude changes depending upon the strength and direction of an applied magnetic field. Each of these characteristics makes EIT an ideal basis for an optical magnetometer [1, 2] which we will demonstrate in later sections of the report. When completed, it should be capable of three dimensional magnetic field mapping down to the picotesla or even femtotesla range. Our current apparatus has the ability to distinguish changes in energy level shifts of .1Hz, which corresponds to 10pT [3], and can be further improved.

Applications for a device of comparable sensitivity span a wide range of different fields and uses, most notably the use of magnetic imaging for diagnostic medicine, in which, an EIT magnetometer would be able to measure the magnetic field generated by nerve impulses while being relatively nonintrusive. For example, such a magne-

tometer would be a much more compact and less expensive alternative to SQUID-based medical magnetometers [4].

1.2 Types of Magnetometers and Their Applications

Magnetometers are used in a wide range of applications including medical imaging, navigation, materials research, computer engineering, and military surveillance. For each of these applications, choosing the correct type of magnetometer is vital to the success of a project. Most devices can be divided into two main groups: vector magnetometers and scalar magnetometers. Scalar magnetometers discern the strength of an unknown magnetic field while vector magnetometers can assess both the magnitude and direction [5]. Most of the magnetometers used today are scalar magnetometers since they tend to be cheaper and easier to manufacture. For precise measurements however, vector magnetometers are generally preferred.

We also need to clarify the definition of a vector magnetometer. The majority of currently available vector sensors are able to measure only a single component of the magnetic field. Thus, a three dimensional vector magnetometer requires three orthogonal sensors to determine the direction of the field. True vector magnetometers that require only one sensor to fully characterize the direction are rare or possibly nonexistent for high sensitivity magnetometers, so they do not receive a special classification. Therefore, the vector magnetometers we discuss in this section are unable to fully map the direction of the magnetic field with a single sensor like our EIT magnetometer.

We now compare high sensitivity vector magnetometers which are commercially available with the expected aptitude of an EIT-based magnetometer. By completing

brief evaluations of popular models, we can determine if a niche exists for an EIT magnetometer in magnetometry.

In Figure 1, we compare the sensitivity of several common vector magnetometers. Our current magnetometer based upon EIT is several orders of magnitude less sensitive than the most precise magnetometers, but field resolution is often not the most important consideration when selecting a magnetometer.

Magnetometer	Max Commercial Sensitivity (T)
GMR	1.00E-08
Fluxgate Magnetometer	1.00E-10
Fiber-optic magnetometer	1.00E-10
Magneto-optical Sensor	3.00E-11
EIT Magnetometer	1.00E-11
Meissner Effect Magnetometer	3.20E-14
Search Coil	2.00E-14
SQUID	1.00E-14

Figure 1: A Comparison of Common High Sensitivity Vector Magnetometers [5,3]

The most sensitive type of vector magnetometers use superconductivity. The two most common types are the superconducting quantum interference device (SQUID) and the Meissner Effect magnetometer.

The SQUID magnetometer is the most precise vector magnetometer currently available. SQUID magnetometers have already been modified for use in biomagnetic applications such as neuron research and medical imaging [4], and they are present in many of the most advanced medical and scientific research. Their extraordinary precision comes from the SQUID's unique method of field measurement. Specifically, it measures periodic current variations in a superconducting ring. The magnetic flux through the superconducting ring generates these fluctuations, so by measuring the output current, the applied field can be deduced. After a demanding modification,

the SQUID magnetometer can create complete vector maps of the field; however, only one vector component is measured in the majority of applications.

The most unique aspect of the SQUID magnetometer is its ability to measure the magnetic field gradient in multiple directions. This feature has been realized by a group at Tampere University of Technology [6]. In addition, a group at Tokyo Denki University has developed a SQUID magnetometer that can measure the second derivative of the field in each direction. Unfortunately, the SQUID magnetometer has a major limitation: It requires temperatures in the superconducting regime to function. This requirement makes the magnetometer bulky despite the small size of the sensor probes. Newer models have raised the required temperature to 77K, which reduces the required size of the device [8]. But, these higher temperature models have lower sensitivity, which limits their utility. Specifically, the SQUID magnetometer functioning at 77K has a sensitivity of $2.8 \times 10^{-13}\text{T}$ which is over an order of magnitude decrease in the sensitivity than when using lower temperatures.

The Meissner Effect magnetometer, like the SQUID magnetometer, needs superconduction to function properly. These magnetometers also measure induced currents in a superconductor [5]. When a superconductor is exposed to a magnetic field, surface currents arise on the surface of the superconductor. These currents cancel the magnetic field inside the superconductor, and the required current for cancellation depends on the magnetic field. This is the Meissner Effect used, and by measuring the current, the magnetic field can be ascertained. Their drawback, like the SQUID magnetometer, is their large size necessary to lower the temperature for superconductivity.

Vector magnetometers based upon induction are some of the most commonly used magnetometers because of their design simplicity and fairly low expense. The Search Coil magnetometer and the Fluxgate magnetometer are two of the most popular induction magnetometers, so we discuss them in detail below.

The Search Coil magnetometer is based on Faraday's Law of induction. The sensitivity of these devices is a function of the number of coils, so they can measure a wide range of magnetic field strengths. However, there exists a wide variation in frequency response [5]. A serious drawback is that Search Coil Magnetometers are not sensitive to DC magnetic fields.

The Fluxgate magnetometer is currently one of the most commonly used magnetometers both in research and industry. The Fluxgate magnetometer is also based on induction, but, in this device, the characteristic of ferromagnetic saturation at high fields is used as well. The downfall for this magnetometer is that the power required to operate this magnetometer is much higher than for the other induction-based non-superconducting magnetometers [5].

We consider one optically-based magnetometer other than our EIT magnetometer, the Magneto-optical sensor. This magnetometer is based upon the rotation of light passing through a magnetic material. The main benefit of this magnetometer is that it has an exceptionally fast response time which is normally in the GHz range [5]. It, like the EIT magnetometer, can be much smaller than many of the other magnetometers due to the increasingly minute size of optical elements.

Magnetometers are also commonly based upon characteristics of special materials. We consider two magnetometers that fall within this category: the Fiber-optic

magnetometer and the Giant magnetoresistance magnetometer (GMR).

The Fiber-optic magnetometer uses magnetostrictive materials as its basis. These materials contract when a magnetic field passes through them. The change in length can be found using a probe laser sent through the fiber optics cable and can be used to calculate the strength of the applied field [5]. The cost for this design is relatively inexpensive, but the fiber optics cable would need to be quite long for high sensitivity. A unique benefit to this device is that the curvature of the magnetic field lines can easily be found by bending the cables.

The GMR magnetometer is another common magnetometers, since it is frequently used as a memory reader for computers [5]. It is based upon the variation in electron scattering rate in a system of two layers of ferromagnetic material, a conductor, and a non-ferromagnetic material.

From this comparison of popular vector magnetometers, we can assess the capabilities of an EIT magnetometer. Our magnetometer would be able to create three dimensional maps of an applied field more easily, for no extra magnetic field sensitive components are necessary. Since the current device can measure in the picotesla to femtotesla range, it would be capable of neural imaging like the SQUID magnetometer, but unlike the currently available medical imaging SQUIDs, all three vector components can be found in one device. The size of this magnetometer will be significantly smaller than any of the superconducting magnetometers due to the size of optical elements. Lastly, the expense would be much lower than for the superconducting magnetometers counterparts. In most applications, sensitivity in the femtotesla range is not necessary, so the benefits of the EIT magnetometer's small

size, vector-mapping ability, and low expense will greatly outweigh the advantages of superconducting magnetometers.

2 Theory

2.1 Overview

The characteristics of Electromagnetically Induced Transparency within a magnetic field will be briefly discussed in the following section. We begin by considering a simple Λ -configuration [8] to observe EIT. Figure 2 shows relevant energy levels for two ground states with an energy difference due to hyperfine splitting and their common excited state. If two coherent light fields with frequencies matching the two atomic transitions shown are sent in, we pump the target atoms into a dark state. This dark state is a coherent, superposition of the two atomic ground states $|g_1\rangle$ and $|g_2\rangle$ [11]. This dark state is non-interacting with the laser fields, so any light passing through the sample atoms is completely transmitted, making them appear transparent.

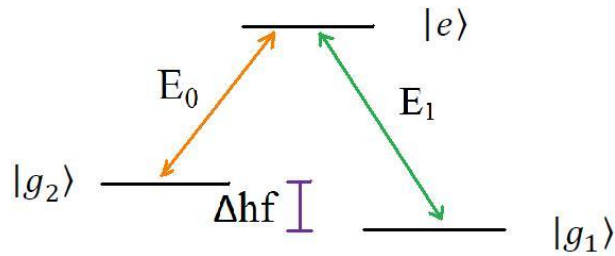


Figure 2: Simple Λ System

We can ascertain why the EIT exists in only a narrow range of frequencies by considering Figure 2 again. If we keep the coherent field E_1 fixed while we vary the frequency of E_2 about the expected resonance frequency, the system is completely non-

interacting only when the frequency is very close to the atomic transition frequency $|g_1\rangle - |g_2\rangle$. If this frequency is sufficiently far from resonance, the dark state has a much smaller probability [1], and there will be mainly absorption of the incident light beam instead of the transmission expected from EIT. To create an optical magnetometer, we need to know how the EIT peaks change due to an applied magnetic field. When an atom is exposed to an external magnetic field, Zeeman splitting breaks the degeneracy in the magnetic quantum states [9], and this splitting is linear with magnetic field strength to a first order approximation [10]. By scanning one of the probe fields, we can find the perturbed frequency separation caused by Zeeman splitting. If both of our laser fields are such that we achieve EIT on the perturbed energy spectrum, we only need to measure the frequency range and amplitude of our EIT signal. With this data, we can deduce the applied magnetic field. Our magnetometer uses a Rubidium vapor as its target, and there are seven different resonances in Rubidium when tuned to the D1 transition as shown in Figure 3.

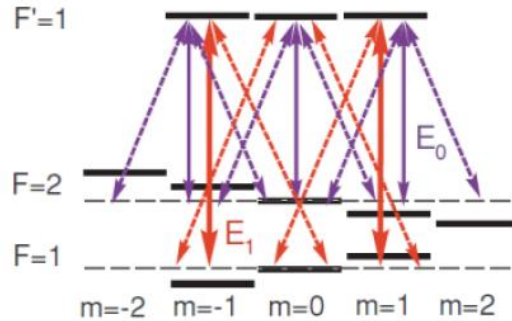


Figure 3: Rubidium 87 Atomic Transitions

Each Λ -system gives a separate transmission peak as shown in Figure 4. The labels $a_{-3}, a_{-2}, \dots, a_3$ are used for convenience when comparing the amplitude and

frequency spacing between transmission peaks. More specifically, the spectral position of the m -th EIT peak is shifted by $\delta_m = m\mu_B \cdot B$ away from the central peak which is magnetoinsensitive.

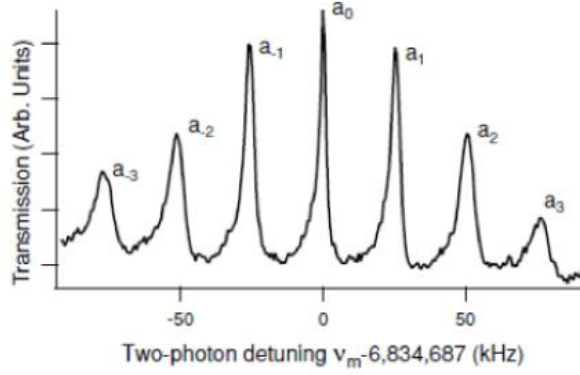


Figure 4: Seven Transmission Peaks for Rubidium 87

The direction of the magnetic field is measured using transition selection rules that determine when a transition is allowed. To find which set of rules to follow, the polarization of the laser fields is compared with the direction of the magnetic field.

2.2 Derivation of the EIT Dark State

At this point, we delve more deeply into the mechanics briefly mentioned in the previous section. First, we derive the dark state and the corresponding bright state. Second, we find the exact conditions required for EIT and how these alter the mechanics of the three level system.

We start by representing the requirements for the Λ -system using the dressed atom Hamiltonian. Figure 5 below is a modified version of Figure 2 including each of the important variables we will consider. This new figure also allows for the condition that the two fields are not on resonance. At this point, no requirements are imposed

on the interaction fields.

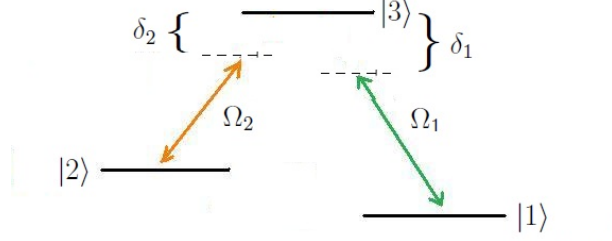


Figure 5: A System in Dressed Atom Basis. Detuning = δ and Rabi frequency = Ω

Our dressed atom Hamiltonian is $H = H_{atom} + H_{photons,1} + H_{photons,2} + H_{interaction}$.

Each of these contributing matrices is written in the basis

$$\{|1\rangle, |2\rangle, |3\rangle\} = \{|g_1\rangle_a |N+1\rangle_{\gamma, \omega_{l,1}} |M\rangle_{\gamma, \omega_{l,2}}, |g_2\rangle_a |N\rangle_{\gamma, \omega_{l,1}} |M+1\rangle_{\gamma, \omega_{l,2}}, |e\rangle_a |N\rangle_{\gamma, \omega_{l,1}} |M\rangle_{\gamma, \omega_{l,2}}\}$$

where N and M are the number of photons dressing the states from the two different laser fields, and γ indicates a photon number state. The index ω_l specifies the frequency associated with the photons and the laser field the photons belong to. We define the bare states as before to be $|g_1\rangle$ for the lower energy ground state, $|g_2\rangle$ for the higher energy ground state, and $|e\rangle$ for the excited state. Each contributing matrix for this system is listed below.

$$H_{atom} = \begin{pmatrix} E_1 & 0 & 0 \\ 0 & E_2 & 0 \\ 0 & 0 & E_3 \end{pmatrix} = \hbar \begin{pmatrix} \omega_1 & 0 & 0 \\ 0 & \omega_2 & 0 \\ 0 & 0 & \omega_3 \end{pmatrix}$$

$$H_{photons,1} = \hbar \omega_{l,1} \begin{pmatrix} N+1 & 0 & 0 \\ 0 & N & 0 \\ 0 & 0 & N \end{pmatrix}$$

$$H_{photons,2} = \hbar\omega_{l,2} \begin{pmatrix} M+1 & 0 & 0 \\ 0 & M & 0 \\ 0 & 0 & M \end{pmatrix}$$

$$H_{interaction} = \hbar \begin{pmatrix} 0 & 0 & \frac{\Omega_1}{2} \\ 0 & 0 & \frac{\Omega_2}{2} \\ \frac{\Omega_1^*}{2} & \frac{\Omega_2^*}{2} & 0 \end{pmatrix}$$

The interaction Hamiltonian shown ensures that the interaction terms couple the correct states. For example, it forbids the $|1\rangle \leftrightarrow |2\rangle$ transition that is unobserved physically. In addition, the interaction terms are $\hbar\frac{\Omega}{2}$ to make sure that the system undergoes Rabi Flopping with the correct frequency Ω_1 due to the first laser field and Ω_2 from the second laser field. Adding together all of the above matrices gives us the full dressed atom Hamiltonian below.

$$H = \hbar \begin{pmatrix} \omega_1 + \omega_{l,1}(N+1) + \omega_{l,2}(M) & 0 & \frac{\Omega_1}{2} \\ 0 & \omega_2 + \omega_{l,2}(M+1) + \omega_{l,1}(N) & \frac{\Omega_2}{2} \\ \frac{\Omega_1^*}{2} & \frac{\Omega_2^*}{2} & \omega_3 + \omega_{l,1}(N) + \omega_{l,2}(M) \end{pmatrix}$$

At this point, we introduce the concept of detuning. Detuning is the frequency difference between an applied laser field and the corresponding atomic transition. For our two laser fields,

$$\delta_1 = \omega_{eg,1} - \omega_{l,1}$$

$$\delta_2 = \omega_{eg,2} - \omega_{l,2}$$

where $\omega_{eg,1} = \omega_3 - \omega_1$ and $\omega_{eg,2} = \omega_3 - \omega_2$. In this notation, δ corresponds to the detuning of a given field, and ω_{eg} is the frequency difference between a given ground state and its excited state. Using these new definitions, the dressed atom Hamiltonian

can be simplified. We set $E_1 = 0$ and subtract $\omega_{l,1}(N) + \omega_{l,2}(M)$ from the diagonal. Both of these operations only shift the background energy level, but only the energy difference between states concerns us here. Next, we set ω_{hf} as the hyperfine splitting frequency between $|1\rangle$ and $|2\rangle$. This gives us the equivalent Hamiltonian shown below.

$$H = \hbar \begin{pmatrix} \omega_{l,1} & 0 & \frac{\Omega_1}{2} \\ 0 & \omega_{hf} + \omega_{l,2} & \frac{\Omega_2}{2} \\ \frac{\Omega_1^*}{2} & \frac{\Omega_2^*}{2} & \omega_{eg,1} \end{pmatrix}$$

Now, we use the rotating wave approximation to subtract $\omega_{l,1}$ from the diagonal to get our final dressed atom Hamiltonian.

$$H = \hbar \begin{pmatrix} 0 & 0 & \frac{\Omega_1}{2} \\ 0 & \delta_1 - \delta_2 & \frac{\Omega_2}{2} \\ \frac{\Omega_1^*}{2} & \frac{\Omega_2^*}{2} & \delta_1 \end{pmatrix}$$

We consider the case where $\delta_1 = \delta_2$ or where the two-photon detuning is zero. The two-photon detuning is defined as the frequency difference between the detuning of two fields or $\Delta = \delta_1 - \delta_2$. We do not yet assume that our laser fields are on resonance. The resulting Hamiltonian is shown below.

$$H = \hbar \begin{pmatrix} 0 & 0 & \frac{\Omega_1}{2} \\ 0 & 0 & \frac{\Omega_2}{2} \\ \frac{\Omega_1^*}{2} & \frac{\Omega_2^*}{2} & \delta_1 \end{pmatrix}$$

The eigenvalues of this matrix are found by solving the equation $\det[H - \lambda I] = 0$ where I is the identity matrix and $[H - \lambda I]$ is a degenerate matrix. This yields the polynomial $0 = -\lambda(\lambda^2 - \delta_1\lambda + \frac{|\Omega_1|^2}{4} - \frac{|\Omega_2|^2}{4})$. The eigenvalues are found to be $\lambda_0 = 0$, $\lambda_{\pm} = \frac{\delta_1 \pm \sqrt{\delta_1^2 + |\Omega_2|^2 - |\Omega_1|^2}}{2}$. The possible states are calculated using the equation $[H - \lambda I]\vec{v} = 0$. In order to examine special cases easily, we can write the new eigenbasis

in terms of the angles θ and ϕ where $\tan \theta = \frac{\Omega_1}{\Omega_2}$ and $\tan 2\phi = \frac{\sqrt{|\Omega_1|^2 + |\Omega_2|^2}}{\delta_1}$ [1]. The new eigenvectors in terms of the old eigenbasis are

$$|a^+\rangle = \sin \theta \sin \phi |1\rangle + \cos \phi |3\rangle + \cos \theta \sin \phi |2\rangle$$

$$|a^0\rangle = \cos \theta |1\rangle - \sin \theta |2\rangle$$

$$|a^-\rangle = \sin \theta \cos \phi |1\rangle - \sin \phi |3\rangle + \cos \theta \cos \phi |2\rangle$$

. We notice $|a^0\rangle$ has no $|3\rangle$ component; therefore, atoms in this state have no probability to be excited. The consequence is that this state is effectively decoupled from the applied laser fields, so $|a^0\rangle$ is called a dark state. Thus, the only requirement for the existence of a dark state in the three-state system is zero two-photon detuning, and we do not need to be on resonance to pump our atoms into a dark state. However, when we are on resonance with both of our laser fields, the atom falls into the dark state much more rapidly [1]. When on resonance, more atoms are excited, thereby increasing the number of opportunities to spontaneously decay into the dark state.

We now consider the case where we are on resonance ($\delta_1 = \delta_2 = 0$). We add in one more condition that $\Omega_1 \ll \Omega_2$. These two are the standard conditions for attaining EIT [15]. Ω_1 is the Rabi frequency of what is normally referred to as the probe field, and Ω_2 corresponds to what is called the coupling field. Under these conditions, we discover $\tan \theta \rightarrow 0$ so $\sin \theta \rightarrow 0$ and $\cos \theta \rightarrow 1$. This makes $|a^0\rangle = |1\rangle$ causing the $|1\rangle$ state to be the same as the dark state. This greatly increases the probability of the atom being pumped into the dark state, so our earlier claim is justified. The other two states in the eigenbasis would be:

$$|a^+\rangle = \frac{1}{\sqrt{2}}|3\rangle + \frac{1}{\sqrt{2}}|2\rangle$$

$$|a^-\rangle = -\frac{1}{\sqrt{2}}|3\rangle + \frac{1}{\sqrt{2}}|2\rangle$$

because on resonance $\tan 2\phi \rightarrow 1$. We notice that the state $|2\rangle$ interacts with the laser fields, so we call this state the bright state. With this information, we have shown that our three-level atom interacting with two coherent fields matching the desired transition frequencies will pump the atom into a dark state, and EIT will be observed.

In order to use EIT, we must understand how the system evolves in time. The main pathway the atom takes is spontaneous emission, an inherently a non-coherent process. This incoherence is due to the universe measuring the photons, collapsing their wave functions. We can use density matrix formalism to handle this incoherence. The form of the density matrix is $\rho = |\Psi\rangle\langle\Psi| = \sum P_i |\Psi_i\rangle\langle\Psi_i|$ where $|\Psi_i\rangle\langle\Psi_i|$ is a statistical mixture of states and P_i is the probability to be in one of these states. The time evolution for any system can be calculated from $i\hbar\frac{d}{dt}\rho = [H, \rho]$, and for our three state atom, we add in decay rates which depend upon many different factors including the detuning, coherence lifetime, and polarization decay. When all of these equations are solved, it can be shown that the line shape of EIT is Lorentzian with respect to the two photon detuning. The equation for the lineshape is given by:

$$f(\Delta) = \gamma \frac{A\gamma + B\Delta}{\gamma^2 + \Delta^2} + C$$

where γ is the width of the resonance, Δ is the two-photon detuning [12]. A,B, and C are fit parameters that we only determine experimentally. The Lorentzian line-shape exists in a narrow two-photon detuning frequency range and has relatively high amplitude, and this is the characteristic EIT peak that we measure experimentally.

2.3 Dependence on the Magnitude of an Applied Magnetic Field

In order to use EIT as an effective magnetometer, we need to know the functional relationship between applied magnetic field and the output signal. As previously mentioned, the applied magnetic field breaks the degeneracy in m quantum numbers causing the well-known Zeeman Splitting. To find the strength of the applied magnetic field, we need to quantify this energy splitting. Since we want our magnetometer to be sensitive to minute fields, we must examine the regime where \vec{B} is small compared to the hyperfine splitting. This gives us an energy shift described by

$$H_{Zeeman} = \frac{\mu_B}{\hbar} g_F \vec{F} \cdot \vec{B}$$

where \vec{B} is the applied magnetic field, $\mu_B = \frac{e\hbar}{2m_e}$ is the Bohr Magnetron, g_F is the g-factor associated with \vec{F} , the total spin operator of the atom ($\vec{S} + \vec{I}$). When we treat the applied magnetic field classically and orient it only along the quantization axis, \hat{z} , we find

$$H_{Zeeman} = \frac{\mu_B}{\hbar} g_F m_F B_Z.$$

The g-factor can be determined using the Wigner - Eckart Theorem that projects the operators \vec{S} and \vec{I} onto the \vec{F} operator. This projection can be used as a substitute for the scalar products within the matrix elements. We find that

$$g_F = g_J \frac{F(F+1) - I(I+1) + J(J+1)}{2F(F+1)} + g_I \frac{F(F+1) + I(I+1) - J(J+1)}{2F(F+1)}$$

where g_J and g_I are the g-factors associated with \vec{J} and \vec{I} . The important feature of this equation is that the splitting is linear with respect to the applied magnetic field so long as the field is small. We can determine the magnetic field by measuring the change in frequency two-photon detuning required to attain EIT. Because of

Zeeman splitting, the two photon detuning required for resonance is offset by $\Delta_0 = \mu_B g_F m_F B_z$, so the formula for the EIT lineshape becomes

$$f(\Delta) = \gamma \frac{A\gamma + B(\Delta - \Delta_0)}{\gamma^2 + (\Delta - \Delta_0)^2} + C.$$

By measuring the new resonance frequency, we can calculate the strength of the applied magnetic field.

2.4 The Effect Due to an Applied Magnetic Field Direction

In order to determine the direction of the applied magnetic field, we use transition selection rules. In our case, we use a linearly polarized beam to drive the transitions, the reason for which will soon be evident. At this stage we are only interested in which transitions exist for a given polarization. The strength of each transition for a given polarization is more difficult to handle analytically, so these strengths will be left to experimental justification. We look at two different cases to motivate the method to determine the polarization of the magnetic field.

With a π -polarized driving electric field we know that the polarization of the field is parallel to the applied field. We find for $L = 0$ that the Rabi Frequency is (neglecting the small \vec{I} term)

$$\Omega = \frac{\mu_B}{\hbar^2} g_s \langle F', m'_F | -e\vec{r} \cdot \vec{E}_{Laser} | F, m_F \rangle.$$

We then set the applied field to be along the quantization axis, \hat{z} , which gives:

$$\Omega = \frac{e\mu_B}{\hbar^2} g_s |\vec{E}_{Laser}| \langle F', m'_F | z | F, m_F \rangle.$$

We find that transitions occur for $\Delta F = 0, \pm 1$ and $\Delta m_F = 0$. Using the solid lines in Figure 3, we find that there are two possible Λ -systems allowed under these conditions.

The second case that we consider is when the driving field is perpendicular to the applied magnetic field (σ - polarized driving field). We find for $L = 0$ (again neglecting the \vec{I} term that

$$\Omega = \frac{\mu_B}{\hbar^2} g_s \langle F', m'_F | xE_x + yE_y | F, m_F \rangle.$$

This can be written using the ladder operators $S_x = \frac{S_+ + S_-}{2}$ and $S_y = \frac{S_+ - S_-}{2i}$ as

$$\Omega = \frac{\mu_B}{\hbar^2} g_s \langle F', m'_F | S_+ E_- + S_- E_+ | F, m_F \rangle.$$

The operators B_- and B_+ correspond to left and right circular polarized light. We find that the allowed transitions are $\Delta m_F = \pm 1$ and $\Delta F = 0, \pm 1$. Using the Rubidium dashed lines shown in Figure 3, we expect three transmission peaks to be observed in this special case. Intermediate polarizations for the driving field between the above two cases would allow each of the possible transitions. Unlike before, the amplitude of the EIT peaks corresponding to the exact value of the matrix elements must be determined to quantitatively find the polarization. In Rubidium, these intermediate polarizations allow all seven possible Λ systems.

3 Experimental Design

In order to achieve a functional, all-optical magnetometer, the following experimental design shown in Figure 6 is used.

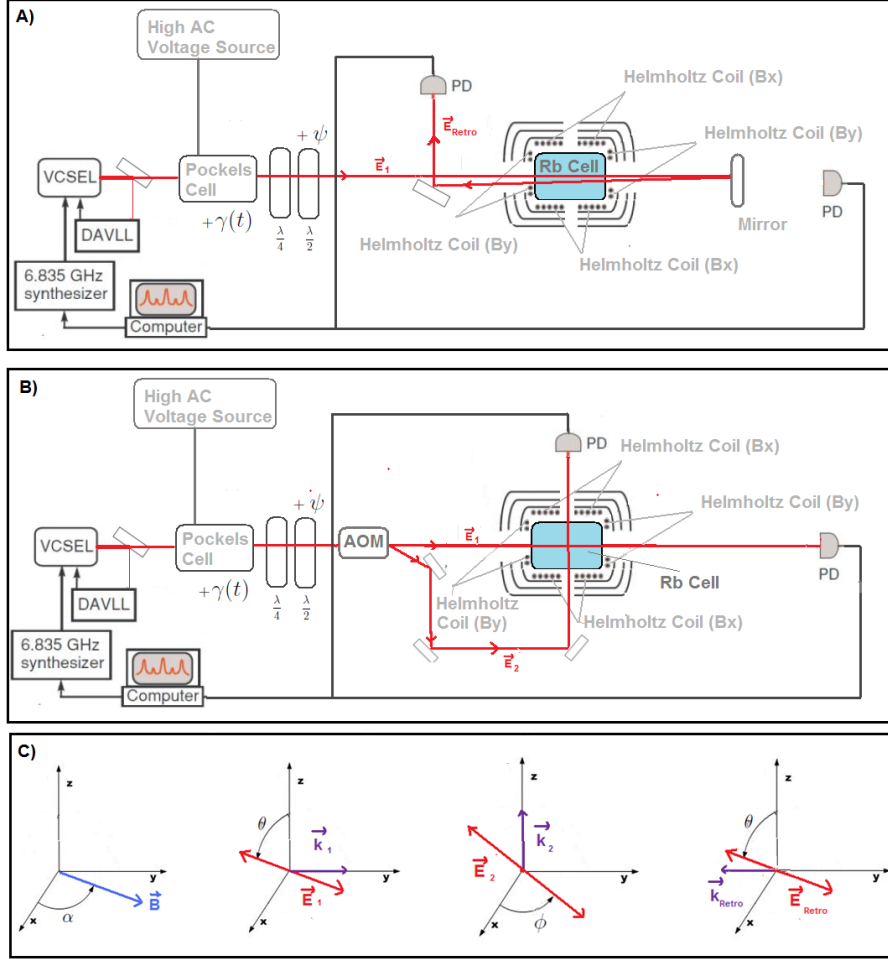


Figure 6: Experimental Design: A) Design for Retro-Reflection Experiment B) Design for Two-Dimensional Measurement of the Magnetic Field Vector C) Coordinates, polarization angles, and propagation vectors for each laser path when inside the Rubidium Cell where $\alpha =$ direction of the applied magnetic field in the $x - y$ plane, θ and ϕ are linear polarizations of the laser paths defined as $\theta = \gamma(t) + \psi$ and $\phi = \gamma(t) + \psi$. The polarization angle $\gamma(t)$ is added from the output from the Pockels Cell and the angle ψ is a linear polarization offset from a $\frac{\lambda}{2}$ waveplate.

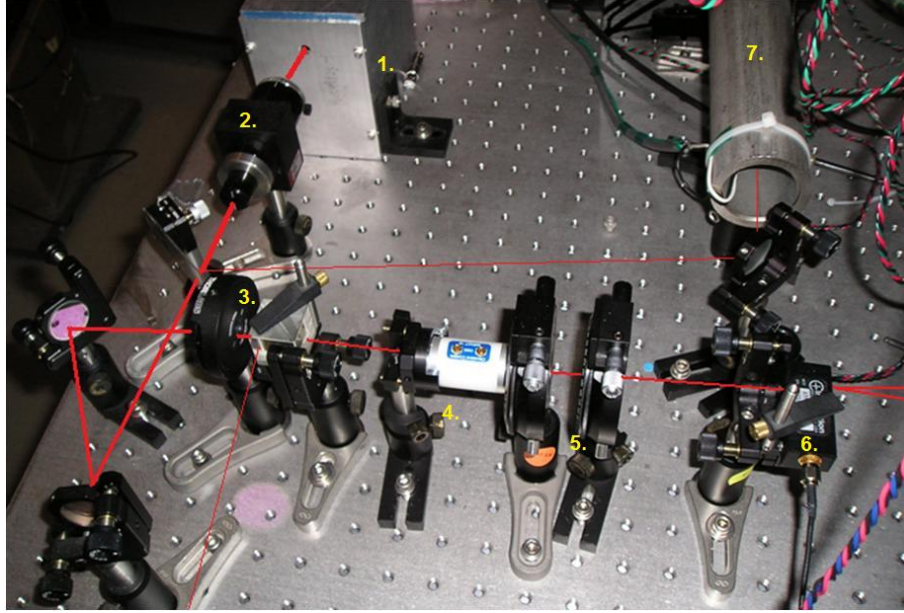


Figure 7: 1. VCSEL 2. Linear Polarizer 3. Laser Power Control 4. Pockels Cell 5. $\frac{\lambda}{2}$ waveplate 6. AOM 7. Magnetic Shield with Rubidium Cell used for DAVLL

3.1 Vertical Cavity Surface Emitting Laser

Since EIT requires two laser fields coupled to a Λ - system, we might assume that we would require two different lasers. Both of these fields must have the same phase and a stable relative frequency, yet lasers drift in these characteristics. This drift makes two independent lasers impractical. If we create two fields with a single laser, the relative frequency and phase will remain the same between the two allowing experimental realization of EIT. For our coherent light source we use a linearly polarized VCSEL. This Vertical Cavity Surface Emitting Laser has a small size, low power consumption, and a tunable frequency. The first two characteristics drastically reduce the space and energy required for our magnetometer. The third allows us to scan the frequency and observe each of the seven Λ - systems in Rubidium 87. The change in laser

frequency is linear with applied current, and current sweeping is the easiest way to modulate the frequency. Another way to tune the frequency of the VSCCEL is through temperature control. The relationship between temperature and frequency output is also linear, but in our case we keep the temperature constant due to the difficulty of rapid temperature change and the control required for frequency modulation.

When we modulate the current supplied to the laser, the laser beam contains not only its original unmodulated frequency, but also many modulation sidebands which are separated in Fourier space by the modulation frequency. As the single laser drifts in phase and frequency, the difference in frequency between each frequency component of the laser remains constant. From the theory section, we know the coupling field must be of lower frequency and larger amplitude than the probe field to gain EIT. We set the carrier frequency and the first sideband frequency of the modulated VSCCEL beam to the required values for the coupling and probe fields to create the conditions required for EIT with a single laser. This means we set the carrier frequency to the $5S_{\frac{1}{2}}, F = 2 \rightarrow 5P_{\frac{1}{2}}, F' = 1$ transition and the first sideband frequency to the value required for the $5S_{\frac{1}{2}}, F = 1 \rightarrow 5P_{\frac{1}{2}}, F' = 1$ transition. We use a computer program to scan the modulation frequency around a set value corresponding to an expected resonance frequency. Due to the way the frequency components were locked, the current modulation frequency is the same as the two photon detuning frequency. When we sweep around the expected resonance frequencies in the presence of an applied magnetic field we observe EIT peaks associated with one of the seven possible Λ -systems. These peaks have the same Lorentzian shape as the line shape function mentioned in the theory section.

3.2 Dichroic Atomic Vapor Laser Lock

The laser's overall frequency must be locked to the transitions of interest. In our case, we want to set the frequency of the laser to the D1 transition line for Rubidium. Since we need to modulate the laser to scan the two-photon detuning, we want a laser lock that does not require any additional laser modulation. Many of the best locking systems use dithering or intentional noise-adding to create an error signal [11]. The benefit of this method is that it creates steep error signals with zero crossings at the desired transition frequency. The main drawback is due to the dithering, for the addition of noise causes the addition of new frequency components in the laser fields [12]. As discussed earlier, we need to control the frequency of modulation as exactly as possible, so this random insertion of noise is undesirable. To get around this problem, we use a laser lock that does not require frequency modulation – the Dichroic Atomic Vapor Laser Lock (DAVLL).

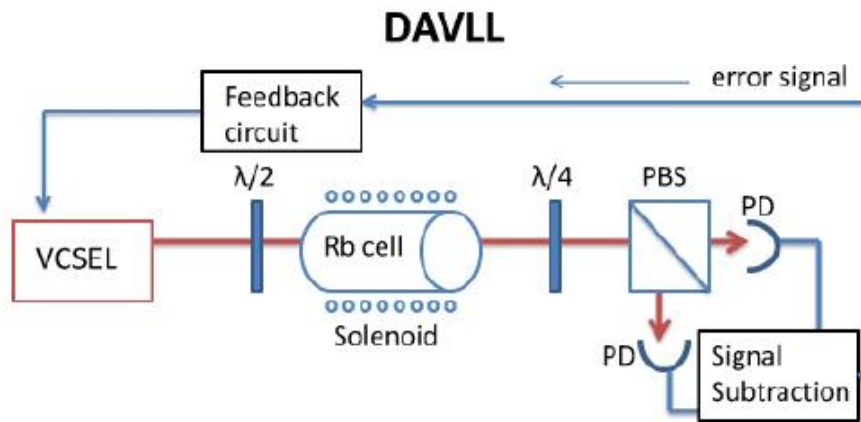


Figure 8: DAVLL System

Figure 8 shows the main components of the laser lock system. We send a small

fraction of the laser light from the VCSEL through a reference cell fitted with natural abundance of Rubidium vapor. This reference cell is placed inside a stack of permanent magnets that produces a magnetic field parallel to the direction of laser propagation. Then, the light passes through a quarter waveplate followed by a polarizing beam splitter (PBS). The two signals obtained on simple photodetectors are subtracted from one another giving an error signal with a zero crossing at the frequency of the D1 transition.

Linearly polarized light can be decomposed into right and left circularly polarized beams as suggested in the Theory section. Due to the PBS, the photodetector output of each arm is proportional to the intensity of either the right or the left circularly polarized light. If we send in the unlocked laser with a frequency around that which is required for transitions $F=1$ to $F'=1$ without an applied magnetic field, the $m_F = \pm 1$ sublevels will be degenerate. This causes both circular polarizations to be equally absorbed, resulting in zero difference between the two photodetector signals for all frequencies. When a magnetic field is applied, these sublevels will no longer be degenerate due to Zeeman Splitting. In this case, one of the circular polarized components will only make transitions to the $m_F = 1$ state, while the other will only make transitions into the $m_F = -1$ state. This means that the center of the absorption line for one polarization component will have a higher frequency than the other [12]. When these two signals are subtracted, they create a dispersion-like error signal with a zero crossing corresponding to the frequency of the desired transition. The strength of the applied magnetic field changes the separation of the m_F sublevels. This, in turn, changes the frequency difference between the two polarization compo-

nents of the light. Therefore, the frequency of the zero crossing, amplitude of the error signal, and the slope changes as a function of the applied magnetic field [12]. The temperature of the Rubidium cell also affects the strength of the error signal. The higher the temperature, the greater the density of Rubidium atoms interacting with the laser, and the more atoms interacting with the laser, the more precise the error signal. The frequency of the lock can easily be altered by changing the location of the zero crossing by rotating the quarter waveplate to cause an offset. By locking to the transition shown in Figure 9, each of the frequency components of the laser (carrier frequency and first sideband) is automatically locked to the specific transitions that satisfy the requirements for EIT.

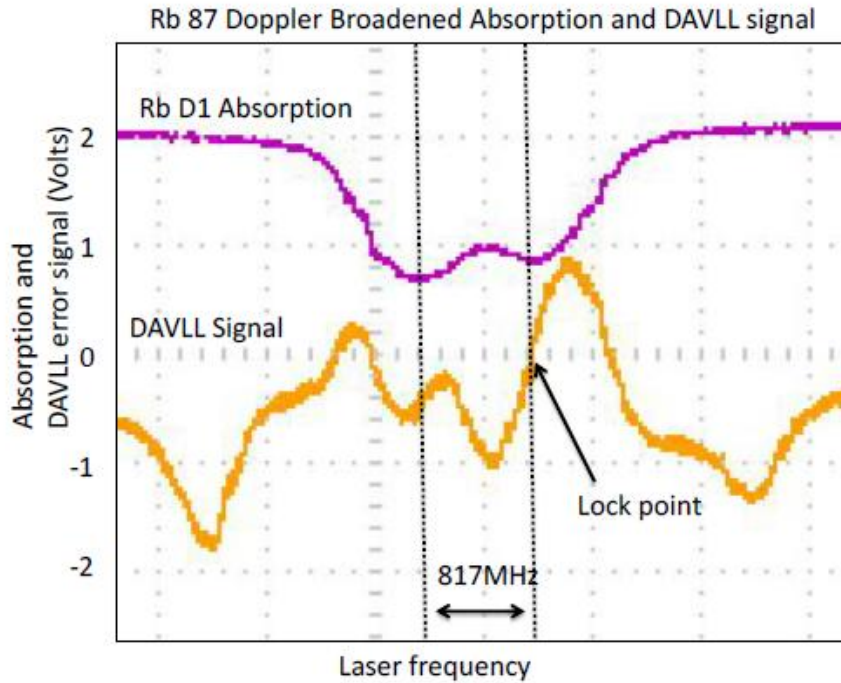


Figure 9: Locking Location on Oscilloscope

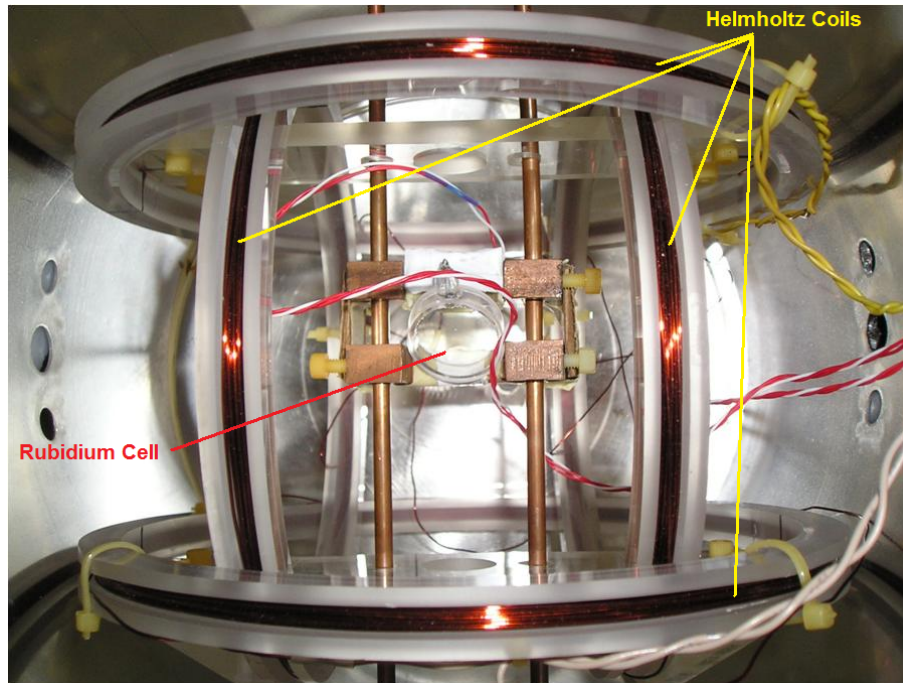


Figure 10: Inside the Magnetic Shield

During an experiment, the majority of the light from our VCSEL is sent through a series of polarizers and waveplates before passing through the experimental cell filled with natural abundance Rubidium. This cell is positioned within a magnetic shield and is maintained at a constant temperature using a heater. For all of these experiments, the temperature was set at 80°C , giving the best EIT transmission signal to noise. By raising the temperature of the cell, we increase the density of Rubidium atoms within the cell, which increases the number of atoms interacting with our laser. At 80°C , the density of Rubidium atoms is 1.2×10^{12} atoms per cubic centimeter. The density of Rb^{87} atoms within the cell is 3.3×10^{11} atoms per cubic centimeter. Two pairs of Helmholtz coils are positioned perpendicular to each other within a magnetic shield, thus allowing us to apply a known magnetic field with two direction components onto our Rubidium sample. The magnetic shield is

formed by three layers of μ -metal that block the external magnetic fields. We also eliminate residual magnetic domains inside the shield to ensure there is no detectable background field. Figure 10 shows the arrangement of the Rubidium cell within the magnetic shield and the two Helmholtz coils. This arrangement allows us to create two vector components of a magnetic field whose magnitudes can be easily calculated from the coil geometry, current, and the position of the Rubidium cell.

For a typical experiment, we set the desired two-photon detuning frequency sweep and observe the Lorentzian EIT peaks on a homemade computer program. From the amplitude of each peak, the direction of the magnetic field can be calculated, and from the frequency separation between adjacent EIT peaks, the strength of the magnetic field can be found.

Data acquisition is accomplished using simple photodetectors that are sensitive to transmission through the Rubidium Cell. These signals are sent directly to our computer for digital data readout or to a lock-in amplifier. An example of a typical experimental run is shown in Figures 11 and 12.

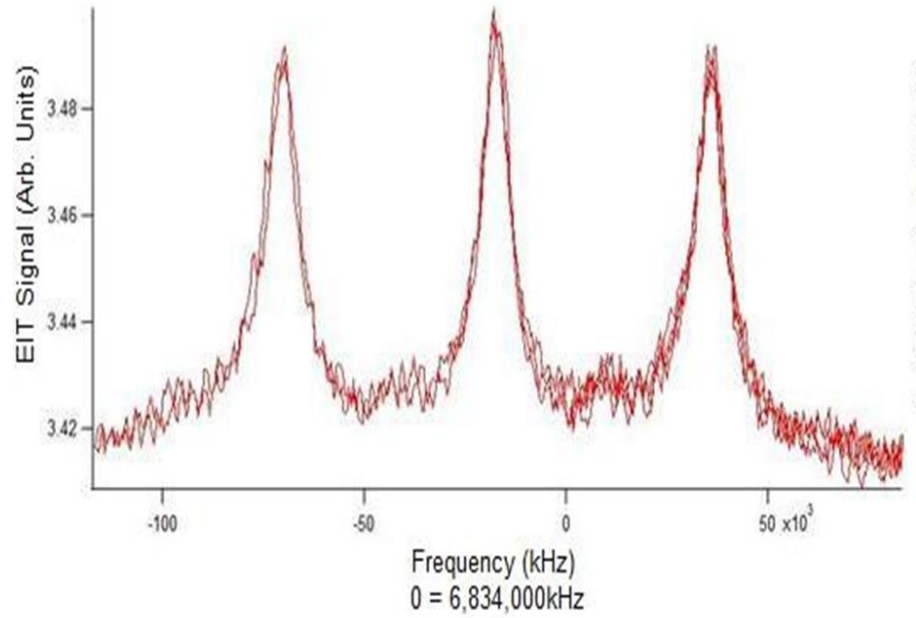


Figure 11: Characteristic EIT Transmission Peaks where the frequency is the two-photon detuning, and the EIT signal is proportional to the voltage detected on the photodetectors. This EIT signal is highest when on resonance and indicates the largest transmission through the sample atoms.

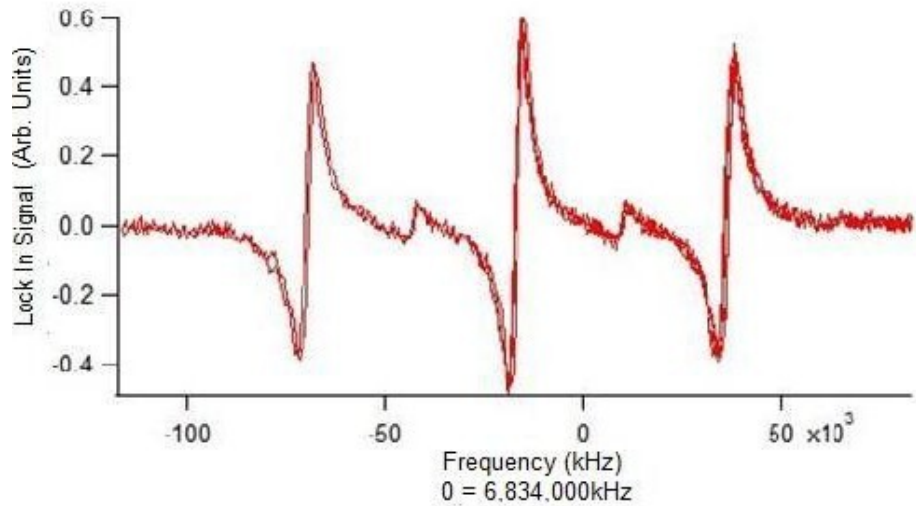


Figure 12: Characteristic EIT Lock In Amplifier Signal

The sharp peaks in Figure 11 are the EIT transmission peaks, and the point where

they are maximum can be seen by the zero crossings in the lock-in signals. The feature to notice about these two graphs is that there are seven EIT peaks, but four of them are completely covered by noise in the transmission graph. However, in the lock-in signal, we can not only see where these small peaks are, but we can also collect useable data from them. Throughout this experiment we rely heavily upon the ability of the lock-in amplifier to detect small signals.

4 Studies on Retro-Reflection Geometry for a Vector Magnetometer

In previous studies with our magnetometer, we have used a transparent target of Rubidium atoms within a magnetic field [2, 3, 10, 13, 14]. This allowed us to measure the EIT on the opposite side of our initial probe field. However, in many applications the target is not transparent, or it cannot be positioned with a measurement device behind it. To see if our magnetometer can handle these applications, we need to see how EIT changes when it is measured on the same side as the incident laser fields. The EIT measurements taken with the incident laser field on the opposite side of the measurement devices will be called single pass, and, on the same side, double pass. This beam is named double pass since the laser is retro-reflected which makes it propagate almost exactly backwards. The laser passes twice through the Rubidium atoms because of this reflection.

The single pass EIT characteristics have been measured in our lab's previous work [2, 3, 10, 13, 14], and have been seen to match the current theory, but the double pass does not have a theoretical model to predict its behavior. To describe its character-

istics we take data that correspond to the behavior seen in the single pass such as the EIT shape, frequency, and amplitude. These are taken at different laser powers, linear polarizations of the laser with respect to the magnetic field, and magnitudes of the magnetic field. We want all of the characteristics of the double pass are the same as the single pass so that our magnetometer can be used in a wide range of practical applications without needing new theoretical models.

For this experiment, we need to reflect our probe laser directly back through the Rubidium cell. Unfortunately, if the beam is reflected along the same path, it interferes with the incident beam, thus distorting the transmission data significantly. We observed that this has a drastic effect upon the shape and existence of transmission peaks. For the two paths to avoid interference, their polarizations would need to be 90 degrees different, but this would change which peaks were visible in the retro-reflected transmission data, as suggested from the selection rules. To get around this problem, the light is reflected in a path that does not overlap with the original path. Since this slight change in position causes a different magnetic field experienced by atoms within the retro-reflected beam's path, the two beams are aligned as closely as possible to mitigate this issue. When the retro-reflected light passed entirely through the cell, we use an edge mirror to divert its path towards a photodetector. By using two photodetectors for transmission data acquisition and a flip mirror for reflection, we are able to switch back and forth between the normal measurement orientation and the retro-reflected orientation. This allows us to make comparisons between the data collected from the two paths.

4.1 Central Peak EIT Frequency

In this experiment, we sweep our probe laser about the expected resonance frequency and compared double pass with single. Any difference in EIT frequency is called a peak shift. In the first peak shift experiment, we alter the linear polarization of our probe laser field using the offset polarization angle ψ defined in Figure 6. Changing the linear polarization of the laser at a constant magnetic field is equivalent to changing the direction of the applied magnetic field at constant laser polarization, which can be seen from the selection rules discussed in the Theory section. However, adjusting the laser polarization is much easier, so it is the method we utilize. In the second experiment, we modify laser power to see if it has an effect on peak shift. At each linear polarization or power of the laser field we fit the transmission amplitude versus frequency for both single and double pass. The linear polarization and power of the laser was determined before the Rubidium cell. We assume that the power is about 20% less for the double pass and that the laser polarization will be unchanged. The frequency of maximum amplitude is called the peak position, and the difference in peak position is called the peak shift. The data collected for the peak shift when changing laser polarization are shown in Figure 13 and when changing laser power are shown in Figure 14.

In order to determine whether or not an experimental run was valid, we use three different types of fits. If the peak position found was significantly different in one of the fit equations, the experimental run is invalid. External noise from changes in background light or fluctuations in laser power and frequency could cause invalidity. Before any measurements were taken, we measured the change in polarization after

the single pass and the drop in laser power after the single pass. This allows us to find more accurate initial conditions for the double pass. The drop in laser power when the field passed through the cell once was found to be 20.4%. To see if the polarization changes significantly within the Rubidium cell we use two polarizers. The first is placed prior to the magnetic shield and the second was placed after. The polarizers are set perpendicular to each other, and we measured the EIT signal. Only background signal is found, suggesting no significant change in polarization when the laser light passes through the Rubidium cell. Both of these results allow us to compare the peak positions as in Figures 13 and 14.

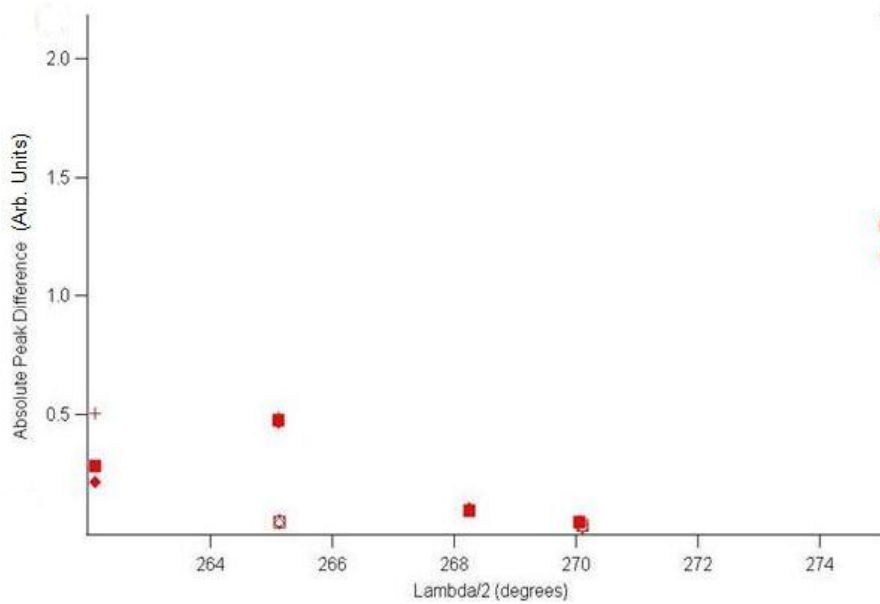


Figure 13: Differences in Peak Frequency Position Differences Due to Polarization (Squares = Gaussian Fit, Diamonds = Lorentzian Fit, Crosses = Parabolic Fit, Solid Shapes = 1st run, Outline Shapes = 2nd run)

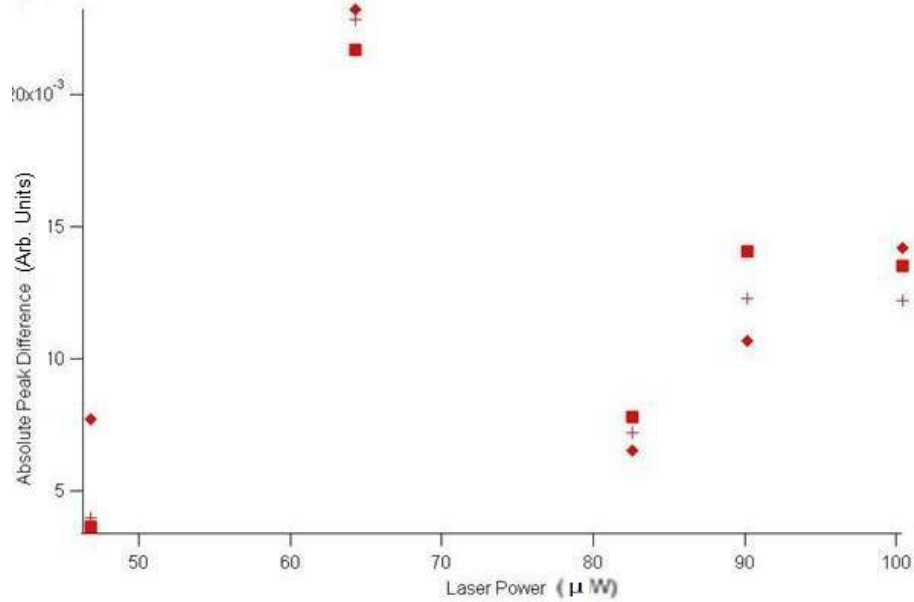


Figure 14: Differences in Peak Frequency Position Differences Due to Laser Power (Same Fits as in 13)

Figures 13 and 14 show that the peak difference is small both when the laser polarization is changed and when the laser power is altered. Even under identical experimental conditions, the EIT signal can change shape or frequency, likely causing the observed differences in peak shift. The y-axis scale for the two plots is different due to the invalid point at 275 degrees in polarization, causing a very large peak difference.

4.2 EIT Peak Characteristics

In this experiment we compare the shape of the central EIT peak of the double pass to the single pass. As in the previous experiment, we collect transmission amplitude data while sweeping laser frequency about resonance. Again, we gather data for both passes at different laser powers. A Lorentzian fit as shown in Figure 15 was used,

and we find no significant change in peak shape when comparing single and double pass EIT peaks at any of the laser powers. Figure 16 shows the percent difference of the EIT peak to the background transmission called contrast. These results are interesting because at higher laser power, the contrast is higher for the double pass. This suggests that the target atoms change atomic state or spatial position slowly enough that the double pass effectively increases the number of interacting atoms, which causes the observed stronger EIT signal. This feature can be used to increase the accuracy of magnetic field measurements by increasing the number of passes through the sample. Looking at the lower power range, we notice that the contrast is less for the double pass. This is because the power dissipates before the double pass, so there is not enough laser power to probe the resonance.

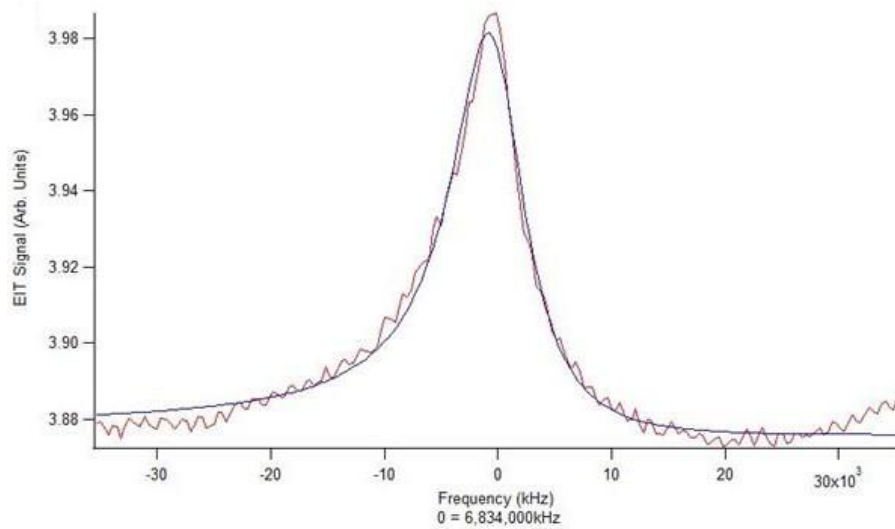


Figure 15: An Example of EIT transmission data fit with a Lorentzian Fit

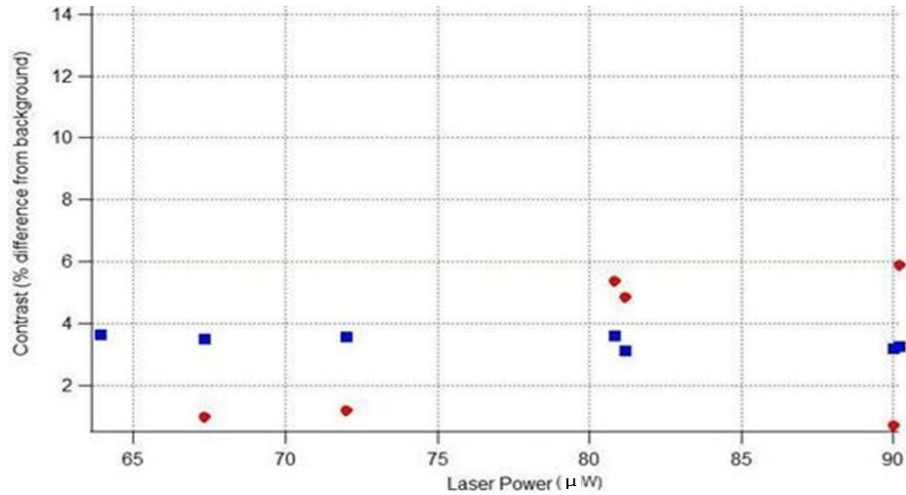


Figure 16: Contrast Comparison Between Single and Double Pass (Squares = Single Pass, Circles = Double Pass)

4.3 EIT Peak Dependence on Polarization

Three different experiments are conducted to describe EIT dependence on laser polarization. Last year, our lab found that there were universal maximums and minimums in transmission when polarization angle θ was changed [10]. An example of these results is shown in Figure 17. In this section, the polarization angle shown along the x -axis is half of the probe laser polarization. So for Figures 17, 18, 19, 20, and 21, the polarization of the laser is twice the angle shown along the x -axis. The values on the x -axis correspond to the angle measured using a half waveplate.

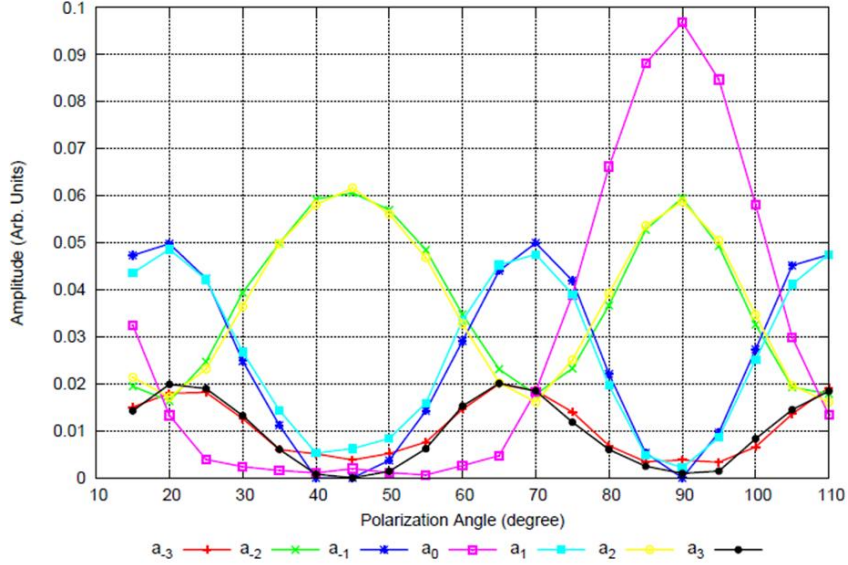


Figure 17: EIT Maximums and Minimums with Polarization [9], a_n designates a specific EIT peak with a_0 indicating the central peak

In the first of these experiments, we manually rotate a $\lambda/2$ waveplate immediately prior to the magnetic shield and collected transmission amplitude as laser frequency is swept about resonance. The contrast versus polarization data collected are shown in Figure 18. We assume that the polarization with the maximum contrast is the polarization of maximum EIT signal. We fit the data with Gaussian fits, and found the peak position for the single pass to be 266 ± 1 degrees, and for double pass 269 ± 1.5 degrees. We see that the maximum position for the double pass is not significantly different from the maximum polarization of the single pass. We attribute the small variation to the inaccuracy of the measurement process since even duplicate polarizations give different results for the contrast due to fluctuations in the laser intensity, the laser frequency, or the room light.

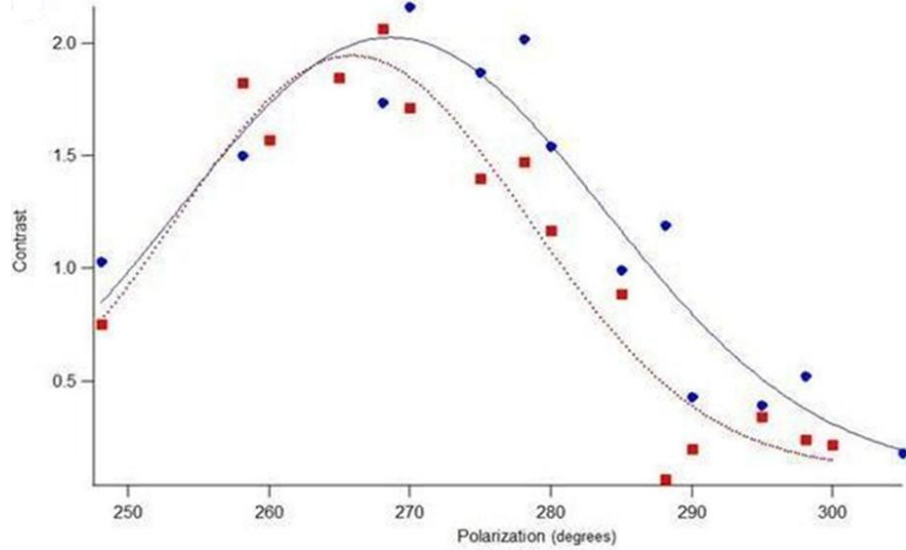


Figure 18: a) EIT signal vs Polarization Using Manual Polarization Change (Squares = Single Pass, Circles = Double Pass) b) EIT Signal vs Polarization Using Polarization Modulation and the Lock in Amplifier

The second and third experiments use a voltage regulated waveplate called a Pockels cell. We calibrate the Pockels cell for a high voltage source, and a linear fit of the calibration curve (shown in Figure 19) makes the determination of the accepted polarization angle (γ) of the trivial. Another benefit of using a Pockels cell is that we can easily sweep the polarization using an input sine wave. In order to get the full spectrum of possible polarization, we manually set a starting angle ψ for the polarization sweep using a half waveplate after the Pockels cell.

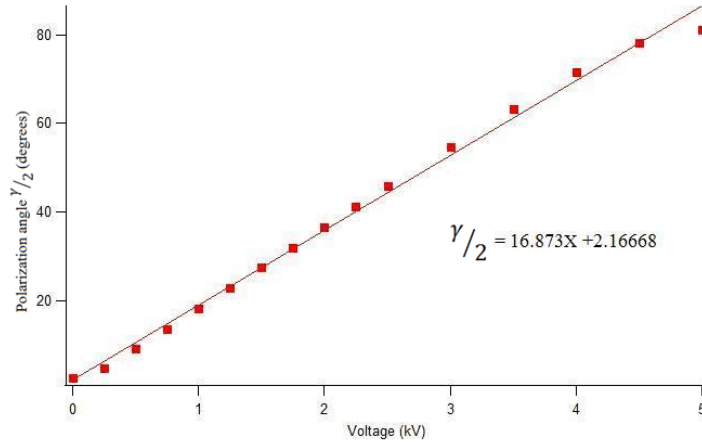


Figure 19: $\frac{\lambda}{2}$ Angle Output Versus Input Voltage for the Pockels Cell

The first method using the Pockels cell sweep sends the modulated polarization signal to the lock-in amplifier, generating a smooth function of polarization. This smooth relationship allows us to find the polarization of maximum and minimum EIT signal. Unfortunately, using polarization modulation, our lock-in amplifier signal is proportional to the entire transmission signal, and not merely the EIT signal. The problem with this is that the background transmission also shifts with polarization, and it is much larger than the EIT signal. The majority of the lock-in signal, therefore, is due to the background. In order to mitigate this problem, we take two lock-in measurements for a single zero point in polarization, one at a frequency where we expect to be on resonance, and another where we do not. Since the background transmission does not depend on the frequency, we subtract the two lock in signals to get the desired EIT signal. We find that there are discontinuous jumps in EIT signal when a different zero point polarization is used, unlike the expected smooth EIT signal versus polarization. So the EIT signal is too small in comparison to the

background noise for our subtraction method to produce meaningful results. The second method for using the Pockels cell exploits the frequency dependence on EIT in a different way. In this procedure, we initially modulate the frequency about the desired EIT signal. The background transmission is not sensitive to this modulation, so the lock in signal appears similar to a derivative of the transmission signal with the background tending to zero. Then we can sweep the polarization using the Pockels cell to get only the EIT shift with polarization and not the background transmission's shift. Figures 20 and 21 show the lock in EIT signal for both the single and double pass using the frequency modulated method. Now we see the expected smooth curve of EIT signal versus polarization unlike with the subtraction method, and we notice that there are polarization positions of maximum and minimum in EIT signal. We want the maximum and minimum positions to be the same for each pass for applications with oblique targets to be practical without major design modifications. Incidentally, we do find that the maximum and minimum are the same for the single and double pass as seen from Figures 20 and 21.

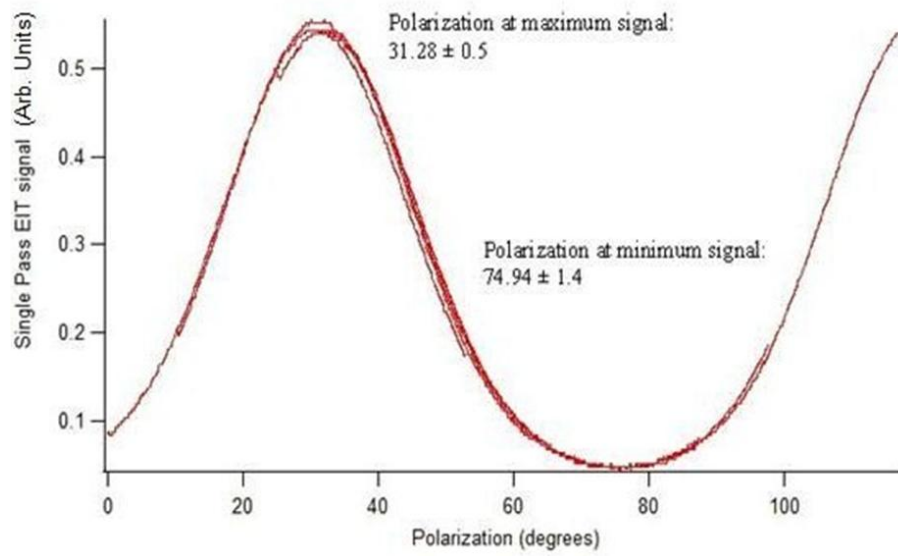


Figure 20: EIT Signal vs Polarization Using Frequency Modulation for Single Pass

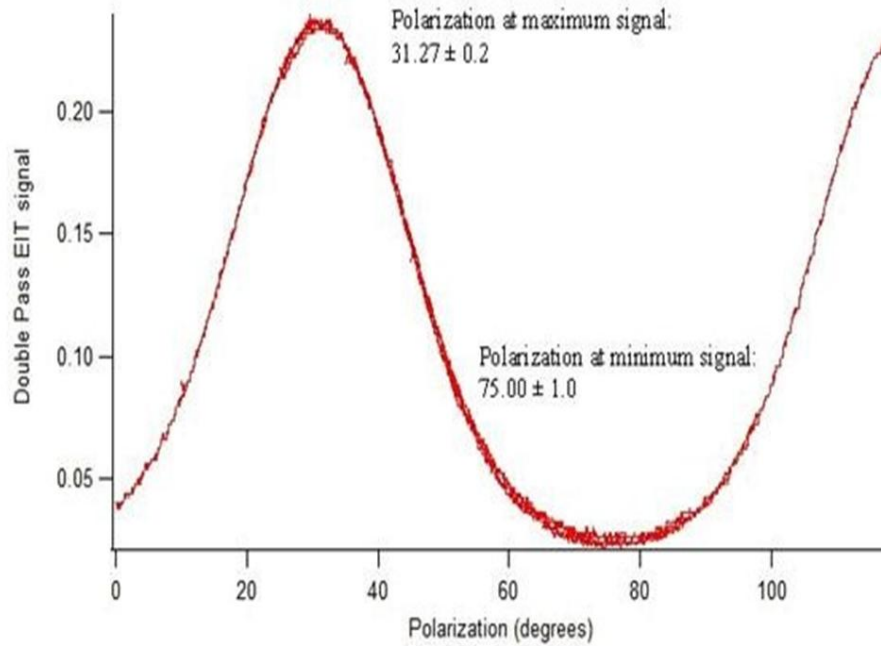


Figure 21: EIT Signal vs Polarization Using Frequency Modulation for Double Pass

5 Two-dimensional Measurement of the Magnetic Field Vector

In our previous experiments, we have only made measurements along a single axis. We can predict the geometric relationship of the laser beam and the magnetic field direction using transition selection rules, but first we construct the coordinate system shown in Figure 22.

In this system, our laser beam propagates in the positive y direction. The angle θ represents the linear polarization of the laser beam, and the magnetic field vector can point in any direction in R^3 . By comparing the polarization of the laser field (θ) and the direction of the magnetic field, we can find a plane that contains both \vec{k} and \vec{B} . An example of a plane containing \vec{k} and \vec{B} is Figure 23. The normal vector to this surface, \vec{n} , is also pictured for reference. We use these normal vectors to accurately determine the direction of the magnetic field, which we discuss later.

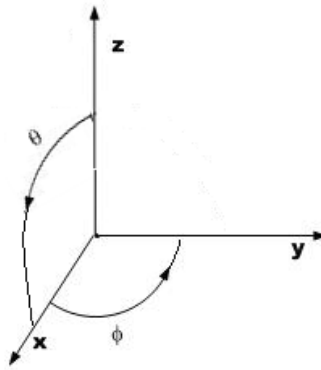


Figure 22: Coordinate System

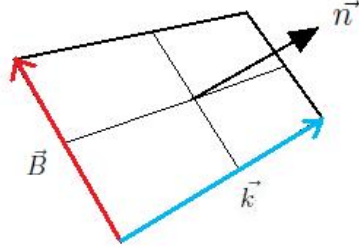


Figure 23: Example plane containing \vec{k} and \vec{B}

To resolve the magnetic field down to a single line, we use a property about two non-parallel planes. The intersection between such planes is a line, and with the correct orientation, we can make this line contain the magnetic field vector.

No matter the direction of propagation of a probe laser, we can find a plane containing both \vec{k} and \vec{B} . When adding a second measurement direction, we ensure that the new plane is not parallel to the plane created from the first measurement. This causes the constraint that the new propagation, \vec{k}_2 , must have the property $\vec{k}_2 \cdot \vec{k}_1 \neq 0$. In other words, \vec{k}_2 cannot be parallel or antiparallel. In our experiment, we choose to make $\vec{k}_2 \perp \vec{k}_1$ for two reasons. The first is that our magnetic shield can accommodate this measurement orientation fairly easily, and the second is that this orientation allows us to assign a natural right handed coordinate system shown in Figure 22. Since \vec{k}_1 propagates along the y -axis, the new propagation vector, \vec{k}_2 is along the z -axis. The polarization of this new laser beam is also linear, and we use the coordinate ϕ to represent it.

We can now motivate the method for measuring the direction of the magnetic field. We know that the cross product between \vec{k} and \vec{B} gives a vector normal to the plane. When the laser polarization is perpendicular to \vec{B} it is parallel to the normal

vector. We construct unit vectors along the direction of the polarization \vec{n}_1 and \vec{n}_2 that are parallel to the vector normal to one of the planes. We know the intersection line between both planes is also inside both planes. This means that it must be perpendicular to the normal vectors of both planes, so it is also perpendicular to \vec{n}_1 and \vec{n}_2 . Therefore, the intersection line is parallel to $\vec{n}_1 \times \vec{n}_2$. Once we calculate this cross product, we know the direction of the magnetic field.

Thus, we modified the apparatus to accommodate this new measurement direction. In order to successfully accomplish this, the two beams must intersect within the Rubidium cell at a 90 degree angle. Since our cell looks like a flat cylinder, the cell must be positioned with a 45 degree angle within the shield (Figure 10 shows the new orientation). To assist with alignment, a paper mask is placed on the face of the Rubidium cell greatly restricting the path of each beam. Due to the design of the magnetic shield, the new beam path propagates vertically. We still wish to use a single laser to supply the fields necessary for EIT, so we need a method to split the beam in two separate paths without reducing the power in each channel (Figure 16). To accomplish this task, we use an Acousto-optic modulator (AOM) which diffracts incident beams depending upon the wavelength of a supplied audio field.

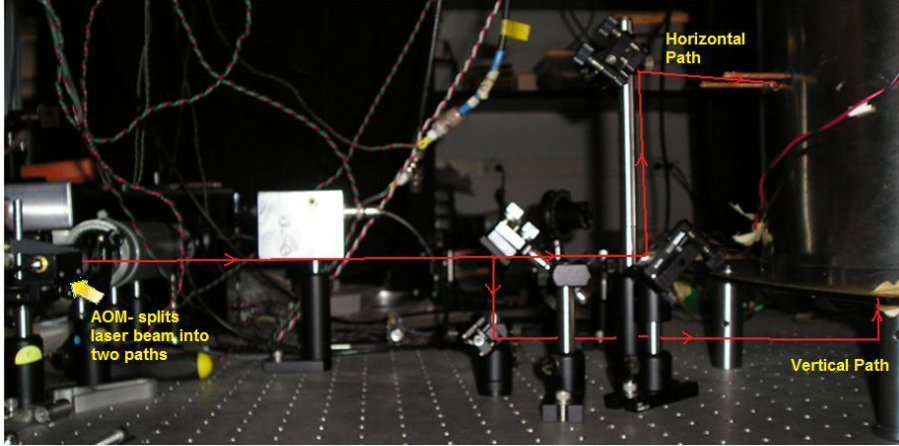


Figure 24: Modification used to measure two vector components of a magnetic field

By supplying the AOM with a sinusoidal input voltage, we can flip between one path and the other with the maximum available intensity. Due to the long lived atomic states of Rubidium, we found that the atomic states are approximately constant if the frequency sent into the AOM is higher than 20kHz. This allows the device to measure both directions of the magnetic field utilizing the maximum possible intensity through both paths at effectively the same time.

5.1 Measurement of the Magnetic Vector Direction

In this experiment, we measure the EIT transmission peak height as a function of laser polarization using the two perpendicular probe directions. For these preliminary measurements, we manually change the polarization of the laser fields using a half waveplate. We use the selection rules for transition probability to determine the direction of the magnetic fields. We use the fact that the laser field is parallel when the a_{-2} and a_2 are maximum while the other peaks are zero, and the laser field is perpendicular when the a_{-2} , a_0 , and a_2 peaks are maximum and the other peaks are

zero.

In each of the experiments, we use a large step size in laser polarization. This causes a significant source of error in the measured direction of the magnetic field, because we do not find the exact polarization of maximum or minimum EIT amplitude.

In the first experiment, we set the magnetic field along the x -axis. The EIT peak height versus laser polarization results for the horizontal measurement beam (along the z -axis) are shown in Figure 25. Results for the vertical measurement beam (along the z -axis) on the same magnetic field are shown in Figure 26.

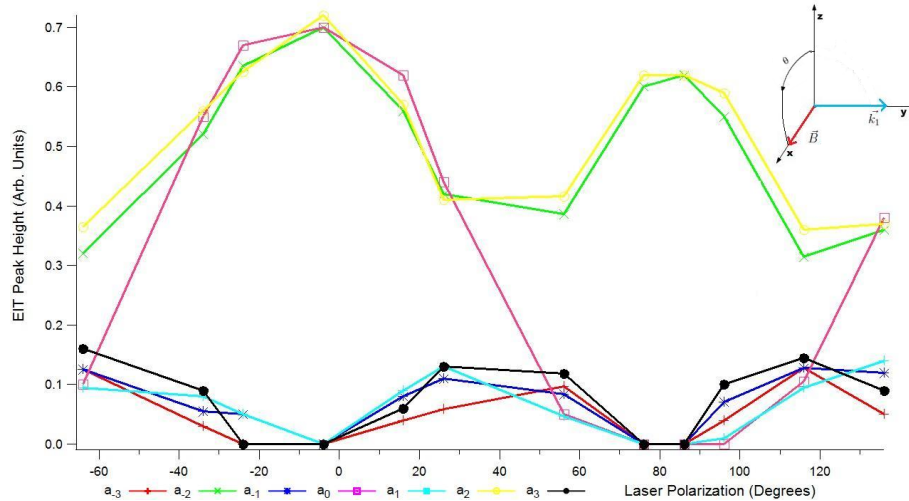


Figure 25: Horizontal Magnetic Field Measurement with a Perpendicular Field

We find from Figure 25 that the laser field is perpendicular to the magnetic field when the polarization is -4 degrees, and it is parallel when the polarization is 88 degrees. We expect to have 0 degrees and 90 degrees, so this rough measurement agrees. From this we know that the normal vector \vec{n}_1 is along the z -axis.

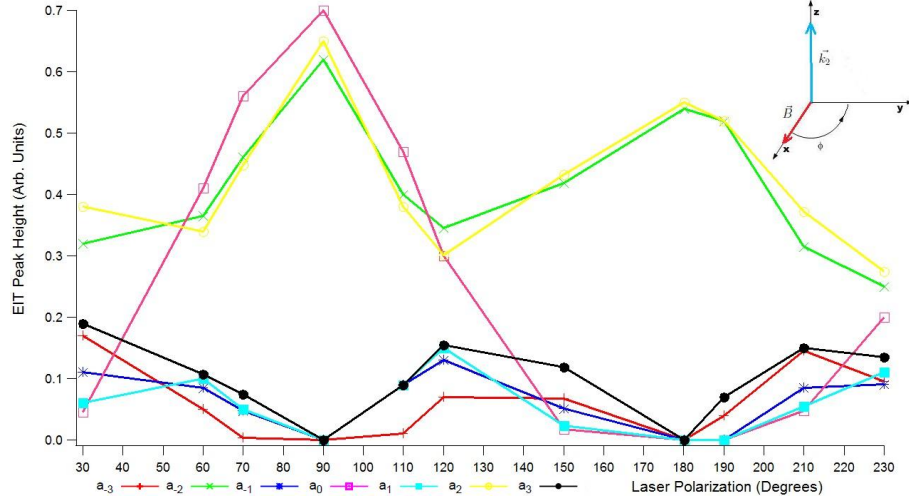


Figure 26: Vertical Magnetic Field Measurement with a Perpendicular Field

We find from the above figure that the laser field is perpendicular when the polarization is 90 degrees, and it is parallel when the polarization is 180 degrees. Therefore, the normal vector to this plane, \vec{n}_2 is along the y -axis. Taking the cross product of \vec{n}_1 and \vec{n}_2 we find that the magnetic field vector lies along the x -axis, as we expect.

In the second experiment, we set the magnetic field along the y -axis. We ensure that the magnitude of the field is the same as the magnitude in the first experiment. We again start with measuring along the y -axis, and the EIT peak height versus laser polarization is shown below.

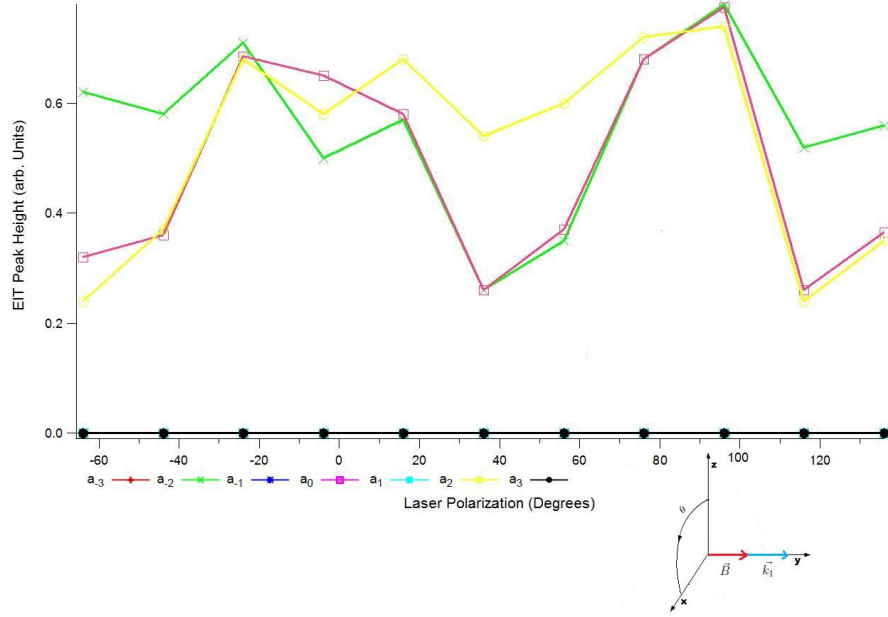


Figure 27: Horizontal Magnetic Field Measurement with a Parallel Field

From Figure 27, we find that the EIT peak height does not have a significant dependence on the polarization of the laser fields. This is because, the a_{-2}, a_0, a_2 peaks remain high throughout the 180 degree span in polarization. Also, the other EIT peak amplitudes remain essentially zero as the polarization changes. From this, we can determine that the magnetic field is approximately parallel to the measurement beam propagation vector. In Figure 28, we measure the same applied magnetic field along the z - axis. In this case, we expect to see a similar dependence of EIT peak height on laser polarization as in Figure 26 because the magnetic field direction is again perpendicular to the propagation direction.

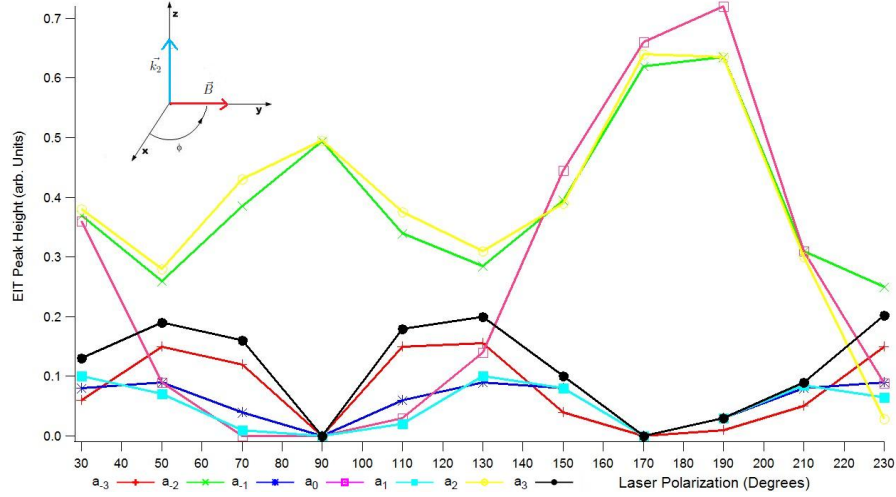


Figure 28: Vertical Magnetic Field Measurement with a Parallel Field

The above figure shows that the magnetic field is perpendicular when the polarization of the laser field is approximately 180 degrees, and it is parallel at about 90 degrees. In this experiment, we have a special case where \vec{k}_1 is parallel to the magnetic field. When this occurs, we automatically know the direction of the magnetic field due to the shape of Figure 27; however, Figure 28 is a useful check that confirms the magnetic field lies along the y -axis.

We now start a new experiment with an applied magnetic field magnetic field oriented at a 45 degree angle from the y -axis but still in the x - y plane. The total span of the polarization was decreased because we need to know a either a perpendicular polarization or a parallel polarization to find the normal vectors.

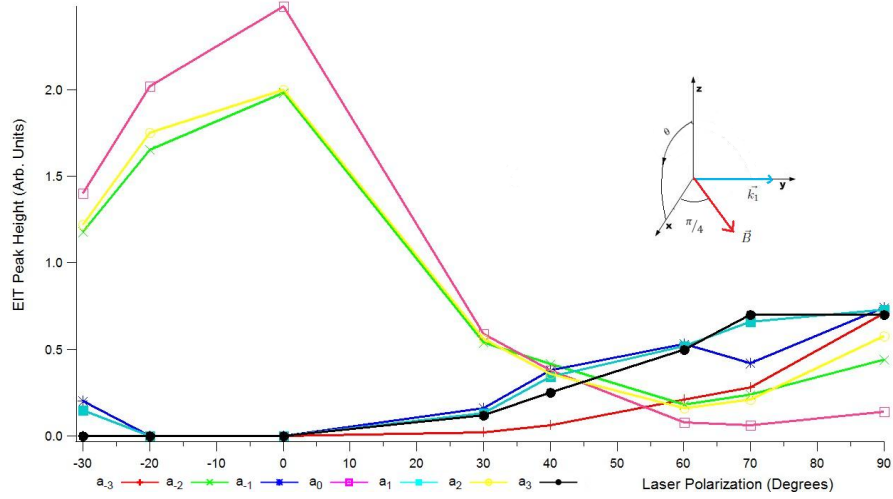


Figure 29: Horizontal Magnetic Field Measurement with a Field Direction at 45 degrees

From Figure 29, we can conclude that the laser field is perpendicular to the magnetic field at approximately 0 degrees. This gives us that the normal vector, \vec{n}_1 , is along the z -axis.

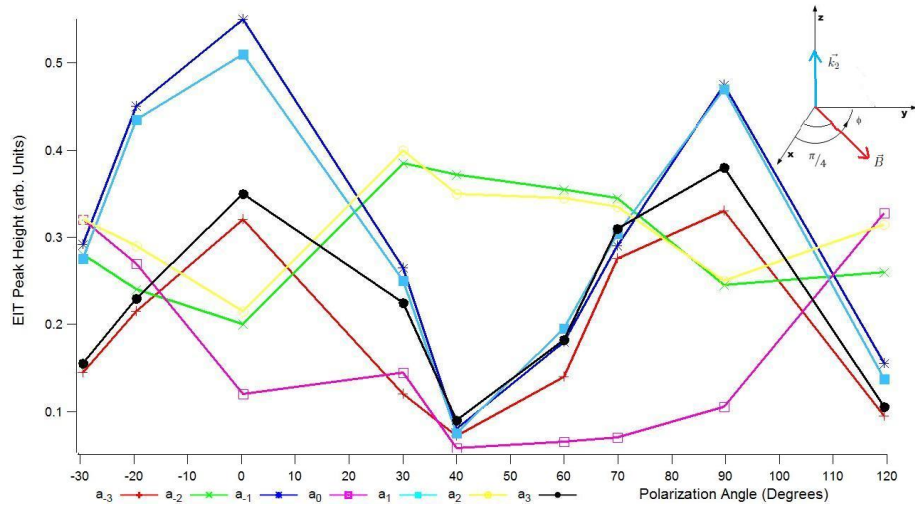


Figure 30: Vertical Magnetic Field Measurement with a Field Direction at 45 degrees

We find from Figure 30 that the laser field is parallel when the laser polarization is around 45 degrees. Thus, we know the polarization is perpendicular when the

polarization is 135 degrees. So, \vec{n}_2 lies in the x - y plane with an angle of 135 degrees. We now take the cross product between \vec{n}_1 and \vec{n}_2 which gives us a vector that lies in the x - y plane with an angle of 225 degrees. We conclude that the magnetic field points at a 45 degree angle and lies in the x - y plane. This matches the expected direction of the magnetic field.

For each of these examples we have been able to roughly determine the direction of an applied magnetic field. This shows that our magnetometer is capable of creating a full vector map of the magnetic field by using two perpendicular measurement directions.

6 Future Experiments

The next step in the development of a fully functional EIT vector magnetometer is to more accurately find the two dimensional vector components of the magnetic field. This will be completed using a similar lock-in polarization sweeping method used to find the maximum and minimum peak heights in the retro-reflection experiment. We will sweep around the EIT maximum for the a_0 peak for both of the measurement orientations. This will provide us with the exact polarization of maximum EIT amplitude which corresponds to the precise direction of the normal vector to the plane containing \vec{k} and \vec{B} .

Next, we will replace each photodetector by a digital camera. By doing this, we will be able to collect EIT maxima and minima on each of the pixels, allowing for an incredibly accurate three dimensional map of the magnetic field.

Another potential step in the our magnetometer developement might be the com-

plete implementation of retro-reflection geometry to create a compact magnetic field sensitive probe. We would then be able to measure unknown magnetic fields outside of our magnetic shield. This would require the creation of a custom made cell containing Rubidium 87 vapor allowing for two perpendicular beams to be retro-reflected prior to measurement. By using fiber optics cables for both measurement directions, we could easily move the cell and collect data for many points in space.

7 Conclusion

In these experiments, we have found that a magnetometer based upon EIT can accurately measure the vector components of an applied magnetic field by measuring in two directions. These results suggest that our apparatus is capable of fully mapping an applied magnetic field. Once our prototype is modified for practical use with unknown magnetic fields, the EIT magnetometer will be a strong competitor with other high sensitive vector magnetometers. The main reason for this is that most of the other highly sensitive magnetometers cannot create complete vector maps.

We also have found through the retro-reflection experiments that our magnetometer can handle applications when the experimenter cannot place a photodetector behind the target whose magnetic field they wish to measure. The reason for this limitation could be the size of the target or the opaqueness of the target. These experiments also verify that a new theoretical model is unnecessary for retro-reflected light since all of the characteristics for non-reflected EIT peaks match those found for retro-reflected EIT peaks. The results we have gained create a strong foundation for the practical ability of a vector magnetometer based upon electromagnetically

induced transparency.

References

- [1] M. Fleischhauer, A. Imamoglu, J. Marangos *Electromagnetically Induced Transparency: Optics in Coherent Media* Rev. Mod. Phys., Vol. 77, April (2005).
- [2] E. E. Mikhailov, I. Novikova, M. D. Havey, and F. A. Narducci, *Magnetic field imaging with atomic Rb vapor* Opt. Lett. 34, 3529-3531 (2009).
- [3] E. E. Mikhailov, T. Horrom, N. Belcher, and I. Novikova *Performance of a prototype atomic clock based on $|\pi\rangle|\pi\rangle$ coherent population trapping resonances in Rb atomic vapor* J. Am. Opt. Soc. B 27, 417 (2010)
- [4] J. Knuutila, S. Ahlfors, A. Ahonen, J. Hällström, M. Kajola et al. *Large Area Lownoise Sevenchannel DC SQUID Magnetometer for Brain Research* Rev. Sci. Instrum. 58, 2145 (1987).
- [5] J. Lenz and A. S. Edelstein *Magnetic Sensors and Their Applications* IEEE Sensors Journal, Vol. 6, No. 3, June (2006).
- [6] M. Burghoff, H. Schleyerbach, D. Drung, L. Trahms, and H. Koch *A Vector Magnetometer Module for Biomagnetic Application* IEEE Transactions on Applied Superconductivity, Vol. 9, No. 2, June (1999).
- [7] L. P. Lee, K. Char, M. S. Colcolugh, and G. Zaharchuk *Monolithic 77 K dc SQUID Magnetometer* Appl. Phys. Lett. 59, 3051 (1991).
- [8] S. E. Harris *Electromagnetically Induced Transparency* Phys. Today 50(7), 36 (1997).

- [9] D. J. Fulton, R. R. Moseley, S. Shepherd, B. D. Sinclair, and M. H. Dunn *Effects of Zeeman Splitting on Electromagnetically-induced Transparency* Optics Communications 116 (1995) 231 -239.
- [10] K. Cox, V. I. Yudin, A. V. Taichenachev, I. Novikova, and E. E. Mikhailov, *Measurements of vector magnetic field using multiple electromagnetically induced transparency resonances in Rb vapor* Phys. Rev. A 83, 015801 (2011).
- [11] G. D. Rovera, G. Santarelli, and A. Clairon *A Laser Diode System Stabilized on the Caesium D2 Line* Rev. Sci. Instrum. 65, 1502 (1994).
- [12] A. Millett-Sikking, I. G. Hughes, P. Tierney, and S. L. Cornish *DAVLL Lineshapes in Atomic Rubidium* J. Phys. B: At. Mol. Opt. Phys. 40 (2007).
- [13] N. Belcher, E. E. Mikhailov, and I. Novikova *Atomic Clocks and Coherent Population Trapping: Experiments for Undergraduate Laboratories*, Am. J. Phys. 77, 988-998 (2009).
- [14] E. E. Mikhailov, I. Novikova, Y. V. Rostovtsev, and G. R. Welch *Buffer-gas Induced Absorption Resonances in Rb Vapor* Phys. Rev. A 70, 033806 (2004).
- [15] A. J. Olson and S. K. Mayer *Electromagnetically Induced Transparency in Rubidium* Am. J. Phys., Vol. 77, No. 2, February (2009).
- [16] M. Scully and M. S. Zubairy *Quantum Optics* Cambridge University Press, Cambridge, U.K. , (1997).